

First-Passage Approach to Optimizing Perturbations for Improved Training of Machine Learning Models

Sagi Meir,^{1, 2} Tommer D. Keidar,^{1, 2} Shlomi Reuveni,^{1, 2, 3} and Barak Hirshberg^{a1, 2, 3}

¹*School of Chemistry, Tel Aviv University, Tel Aviv 6997801, Israel.*

²*The Center for Physics and Chemistry of Living Systems, Tel Aviv University, Tel Aviv 6997801, Israel.*

³*The Center for Computational Molecular and Materials Science, Tel Aviv University, Tel Aviv 6997801, Israel.*

Machine learning models have become indispensable tools in applications across the physical sciences. Their training is often time-consuming, vastly exceeding the inference timescales. Several protocols have been developed to perturb the learning process and improve the training, such as shrink and perturb, warm restarts, and stochastic resetting. For classifiers, these perturbations have been shown to result in enhanced speedups or improved generalization. However, the design of such perturbations is usually done *ad hoc* by intuition and trial and error. To rationally optimize training protocols, we frame them as first-passage processes and consider their response to perturbations. We show that if the unperturbed learning process reaches a quasi-steady state, the response at a single perturbation frequency can predict the behavior at a wide range of frequencies. We employ this approach to a CIFAR-10 classifier using the ResNet-18 model and identify a useful perturbation and frequency among several possibilities. We demonstrate the transferability of the approach to other datasets, architectures, optimizers and even tasks (regression instead of classification). Our work allows optimization of perturbations for improving the training of machine learning models using a first-passage approach.

Keywords: machine learning, neural networks, perturbations, stochastic resetting, first-passage, response theory

I. INTRODUCTION

Machine learning algorithms and deep neural network (NN) models have become powerful tools across chemistry and physics to tackle challenges that were once computationally or experimentally prohibitive. Examples include protein structure prediction [1], entropy calculation for physical systems [2], machine learning potentials [3], and many others [4–13]. Unfortunately, these capabilities come with a time-consuming price spent on model training. Second-order optimization algorithms are unfeasible for deep NN [14, 15], and currently, stochastic gradient descent (SGD) [15–17] and its variants [18–20], remain a cornerstone of NN training [21, 22].

SGD by itself can be slow and prone to getting stuck in local minima. Several common practices are used to address these limitations. First is the incorporation of momentum and adaptive learning rates as done by modern optimizers, usually leading to faster convergence and improved performance [19, 20, 22, 23]. The second, which is the focus of this work, is to “perturb” the training process, which may lead to speedup or improved generalization. Examples include shrink & perturb (S&P) [24, 25], warm restarts [15], stochastic resetting (SR) [26] and continual backpropagation [27].

Ash et al. [24] first suggested the S&P protocol to improve generalization during online learning. More recently, Zaidi et al. [25] investigated when such re-initialization might help the training, and concluded that while it is clear S&P is helpful in some cases, a general theory of why it works is missing. Bae et al. [26] applied SR to a dynamically-updated checkpoint during the training of an NN with a resetting time sampled from an exponential distribution. They concluded that their strategy decreases overfitting on noisy labels and leads to better generalization. Yet, predicting the optimal resetting rate *a priori* was not possible. Loshchilov et al. [15] showed that a protocol with warm restarts converges up to four times faster to the same test accuracy compared to standard SGD training. Overall, despite their usefulness, a theory capable of predicting the effect of such perturbation protocols is missing, and their design is often done by intuition and empirical trial and error.

The resemblance of SGD to Langevin dynamics [28–30] has been utilized to describe and analyze the learning process of NNs with concepts and methods from thermodynamics [31] and statistical physics [32–36]. For example, Feng et al. found an inverse fluctuation-dissipation relation between weights’ fluctuations and the flatness of the loss landscape. Based on their finding, they developed an algorithm that delays catastrophic forgetting in sequential learning tasks [28].

^a Author to whom any correspondence should be addressed hirshb@tauex.tau.ac.il

Another example is the work of Stephan et al. where they showed that SGD with a constant learning rate can be used as an approximate Bayesian posterior inference algorithm [37]. Their result was obtained by viewing SGD as a Markov chain with a stationary distribution. However, despite the advancements in applying statistical mechanical tools in machine learning, they have not been previously used to design perturbations to improve the performance of SGD optimizers.

Recently, Keidar et al. developed a response theory to predict how rare perturbations affect the completion of an arbitrary stochastic process [38]. Their theory focused on first-passage processes [39–41], in which a stochastic process has a predefined distribution of initial conditions and a well-defined target. The stochastic nature of the process gives rise to a distribution of first-passage times, i.e., the first time the process reaches its target. In this work, we treat the SGD-based training of NNs up to a predefined target accuracy as a first-passage process. We treat protocols such as S&P, warm restarts, and stochastic resetting as perturbations to the first-passage process that occur every P epochs during the training. We employ the theory of Keidar et al. for the first time to analyze and improve the training of NN models using such perturbations. We show that, given a set of protocols, we can determine which would lead to the highest acceleration and identify the optimal perturbation time interval P . We focus on three types of protocols: S&P, partial re-initialization of small weights (partial SR), and full SR. Finally, we suggest a methodology for testing and analyzing new perturbation protocols. We demonstrate the transferability of the approach across datasets (CIFAR-10, CIFAR-100 [42] and MNIST [43]), architectures (ResNet-18 [44] and fully-connected NN), optimizers (SGD, SGD with momentum, Adam [20]) and even tasks (classification and regression) in the supporting information.

II. THEORY

In this work, we treat the NN training in the absence of a perturbation as a stochastic process that is characterized by a propagator $G(\boldsymbol{\theta}, t)$, representing the probability of being in state $\boldsymbol{\theta}$ at time t . We emphasize that $\boldsymbol{\theta}$ characterizes the overall state of the system, i.e., it may represent the weights, biases, hyperparameters, etc. We focus on first-passage processes (see Fig. 1A), and define the first-passage time (FPT) as the first instance in which the test accuracy reaches a certain threshold, which is treated as an absorbing boundary condition. Namely, once the test accuracy of a model reaches the target, training is stopped. Since it is a stochastic process, there will be an FPT distribution. We denote with T the random variable representing the FPT of the unperturbed training process. We define the survival probability $\Psi_T(t) \equiv \Pr(T > t)$ as the fraction of models which did not reach the threshold at time t . Note, that $\Psi_T(t)$ is one minus the cumulative distribution function (CDF) of T . In terms of the propagator, the survival probability can be written as

$$\Psi_T(t) = \int_{\Theta} G(\boldsymbol{\theta}, t) d\boldsymbol{\theta}, \quad (1)$$

where Θ symbolizes that the integration domain is over all possible states.

Fig. 1B shows the training process with a perturbation that is applied every P epochs. We denote by T_P the random variable representing the FPT of the perturbed process to the target accuracy. The perturbation can be of any form, e.g., it can affect the network weights, hyperparameters, activation functions, or any other component of the training. Keidar et al. showed that the perturbed FPT is connected to the unperturbed FPT through [38],

$$T_P = \begin{cases} T & \text{if } T \leq P, \\ P + \tau_P(\boldsymbol{\theta}) & \text{if } T > P, \end{cases} \quad (2)$$

where $\tau_P(\boldsymbol{\theta})$ is the random variable representing the residual number of epochs it takes to reach the target after the perturbation has been first applied (see Fig. 1B). It depends on $\boldsymbol{\theta}$, the state of the network at time P , which might be different for every realization of the process.

Applying the law of total expectation to Eq. (2) (see the derivation in the supporting information), we obtain the mean FPT under perturbations, $\mathbb{E}[T_P]$,

$$\mathbb{E}[T_P] = \sum_{t=0}^{P-1} \Psi_T(t) + \Psi_T(P) \bar{\tau}_P, \quad (3)$$

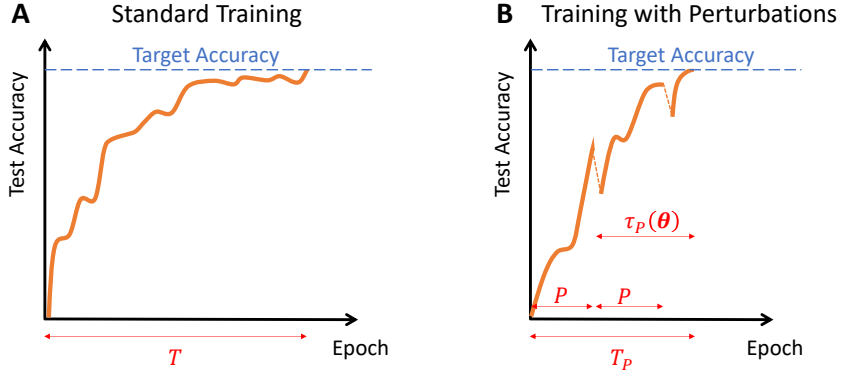


Figure 1. Training NNs as a first-passage process. Panel A presents the test accuracy as a function of the number of epochs for training without perturbations (orange line). Here, T is the FPT to reach the target accuracy (dashed blue line). Panel B presents the test accuracy as a function of the number of epochs for training with a perturbation every P epochs (orange line). T_P is the perturbed FPT to the target accuracy (dashed blue line) and $\tau_P(\boldsymbol{\theta})$ is the residual time to reach the target accuracy after the first perturbation.

where $\bar{\tau}_P$ is given by

$$\bar{\tau}_P = \int_{\Theta} \mathbb{E}[\tau_P(\boldsymbol{\theta})] \frac{G(\boldsymbol{\theta}, P)}{\Psi_T(P)} d\boldsymbol{\theta}. \quad (4)$$

In Eq. (4), $\mathbb{E}[\tau_P(\boldsymbol{\theta})]$ is the average residual time after the first perturbation over all possible noise realizations of the stochastic training process after the perturbation was applied to a given state $\boldsymbol{\theta}$ at time P . Hence, $\bar{\tau}_P$ can be understood as the average of $\mathbb{E}[\tau_P(\boldsymbol{\theta})]$ over all possible $\boldsymbol{\theta}$ generated by the unperturbed process at time P right before the perturbation has been applied.

Eq. (3) formally decomposes the mean FPT with the perturbation to two contributions. The first term, $\sum_{t=0}^{P-1} \Psi_T(t)$, sets a lower bound on $\mathbb{E}[T_P]$ that only depends on the unperturbed process. The second term encodes all the effects of the perturbation on the mean FPT. These equations allow, in principle to predict the effect of a perturbation on the training for all P .

Consider, for example, the specific case of SR as the perturbation [45–49]. Then, every P epochs, the state of the system is restarted by resampling the initial conditions for training. As a result, for any training process, $\tau_P(\boldsymbol{\theta})$ does not depend on the state at time P , and is simply an independent and identically distributed copy of T_P . In that case, $\bar{\tau}_P = \mathbb{E}[T_P]$, and substituting it into Eq. (3) gives [50],

$$\mathbb{E}[T_P]_{SR} = \frac{1}{1 - \Psi_T(P)} \sum_{t=0}^{P-1} \Psi_T(t). \quad (5)$$

Eq. (5) shows that, for SR, the mean FPT with the perturbation can be predicted entirely from the survival probability of the unperturbed learning process. To derive Eq. (5), we used the specific properties of SR. For other perturbations, one must assume something about the dynamics of the underlying training process as we do in the next section.

III. RESULTS AND DISCUSSION

A. Quasi-steady state leads to P -independent residual times

To proceed beyond Eq. (3), we consider a stochastic process in which the propagator reaches a quasi-steady state (QSS) after a typical relaxation time t_r ,

$$G(\boldsymbol{\theta}, t) \simeq \phi(\boldsymbol{\theta}) \Psi_T(t) \quad \text{for } t > t_r. \quad (6)$$

In Eq. (6), $\phi(\boldsymbol{\theta})$ is a time-independent probability density function of the network state $\boldsymbol{\theta}$. In other words, a QSS is defined by constant relative populations of all states $\boldsymbol{\theta}$, although the overall number of models that survived declines over time through $\Psi_T(t)$ [51], as illustrated in Fig. 2. The QSS approximation is commonly applied to analyze chemical kinetics [51–55], but has not been used to explain NN training before.

A QSS could also emerge during the training of certain NNs, for example, through a separation of timescales in learning. Typically, the training loss drops rapidly in the early stages of learning, and a much slower decrease in loss is observed at later stages while training accuracy plateaus [28]. In other words, the state of the network evolves rapidly at first, but later the model approaches a local minimum of the loss landscape leading to smaller gradient updates of the parameters. This suggests that beyond a characteristic relaxation time, the state of the network becomes approximately stationary. Next, we show that in this case, i.e., when a QSS emerges, the mean residual time $\bar{\tau}_P$ becomes independent of the perturbation epoch P , provided it is rare. As a result, we can predict the mean first-passage time (FPT) across a wide range of perturbation frequencies by sampling the training process at a single frequency.

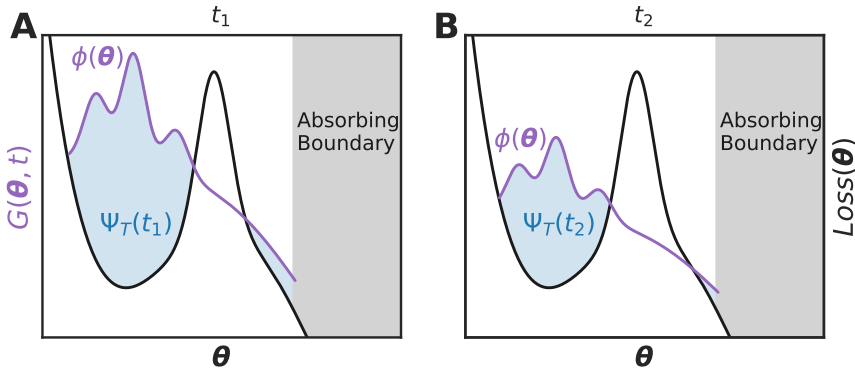


Figure 2. An illustration of a QSS of a propagator $G(\boldsymbol{\theta}, t)$ at times $t_2 > t_1 > t_r$. At QSS, the probability density function $\phi(\boldsymbol{\theta})$ (purple lines) maintains the same shape, while the fraction of models that survived (blue areas) declines over time through panels A-B, i.e., $\Psi_T(t_1) > \Psi_T(t_2)$.

To show this, we consider three timescales in the system: the relaxation time t_r , the perturbation time interval P and the mean residual time $\bar{\tau}_P$. Considering a perturbation that is done at a time $P > t_r$, and utilizing QSS, we observe that the perturbation acts on a state sampled from $\phi(\boldsymbol{\theta})$ irrespective of P . We can then plug Eq. (6) into Eq. (4) and get

$$\bar{\tau}_P = \int_{\Theta} \mathbb{E}[\tau_P(\boldsymbol{\theta})] \phi(\boldsymbol{\theta}) d\boldsymbol{\theta}. \quad (7)$$

Note that the mean residual time for completion after the perturbation is applied still depends on P through $\mathbb{E}[\tau_P(\boldsymbol{\theta})]$. Next, if the perturbation is rare enough, i.e., $P > \bar{\tau}_P$, we effectively perturb the system only once on average before the training is complete. As a result, $\tau_P(\boldsymbol{\theta}) = \bar{\tau}(\boldsymbol{\theta})$, i.e., does not depend on P , leading to

$$\bar{\tau}_P \approx \bar{\tau} = \int_{\Theta} \mathbb{E}[\tau(\boldsymbol{\theta})] \phi(\boldsymbol{\theta}) d\boldsymbol{\theta} \quad \text{for } P > \max(t_r, \bar{\tau}_P). \quad (8)$$

Plugging Eq. (8) into Eq. (3) leads to

$$\mathbb{E}[T_P] = \sum_{t=0}^{P-1} \Psi_T(t) + \Psi_T(P) \bar{\tau}. \quad (9)$$

Eq. (9) sets the recipe for designing useful perturbations and the frequencies at which to apply them. It tells us to perform simulations applying the perturbation only once at some $P^* > \max(t_r, \bar{\tau}_P)$. These simulations provide

the unbiased survival function until time P^* and $\bar{\tau}$. Combining the two, we can predict the mean FPT for all values $\max(t_r, \bar{\tau}_P) \leq P \leq P^*$.

Below, we first test the QSS hypothesis when training a CIFAR-10 [42] classifier using the ResNet-18 model [44]. Then, for two perturbations, S&P and partial SR, we show that indeed $\bar{\tau}_P \approx \bar{\tau}$ for a wide range of P . Finally, we use Eq. (9) to predict the mean FPT under these perturbations at a wide range of P , and benchmark them against brute-force training. We show that this procedure can be used to select a perturbation and time interval P that lead to faster training.

B. Experimental test of the quasi-steady-state

A naive approach to demonstrate a QSS when training an NN model would be to sample several learning trajectories while keeping track of the parameters to obtain $G(\boldsymbol{\theta}, t)$. However, it is impractical to keep track of millions of parameters, and the finite sample size introduces noise to the estimation of the distribution of $G(\boldsymbol{\theta}, t)$. This noise increases with the dimensionality of $\boldsymbol{\theta}$, making it infeasible to demonstrate a QSS convergence from the trajectory data of $\boldsymbol{\theta}$. Instead, we draw inspiration from enhanced sampling of free energy surfaces [56–58] and define a collective variable, $A(\boldsymbol{\theta})$, representing the state of the system and look at its marginal distribution,

$$G(A, t) = \int_{\Theta} G(\boldsymbol{\theta}, t) \delta(A(\boldsymbol{\theta}) - A) d\boldsymbol{\theta}. \quad (10)$$

In practice, we will use the test set accuracy as a collective variable. If $G(\boldsymbol{\theta}, t)$ reaches a QSS, and we plug Eq. (6) into Eq. (10), we get a QSS also in $G(A, t)$,

$$G(A, t) \simeq \Psi_T(t) \int_{\Theta} \phi(\boldsymbol{\theta}) \delta(A(\boldsymbol{\theta}) - A) d\boldsymbol{\theta} = \Psi_T(t) \phi(A), \quad \text{for } t > t_r. \quad (11)$$

In Eq. (11), $\phi(A) = \int_{\Theta} \phi(\boldsymbol{\theta}) \delta(A(\boldsymbol{\theta}) - A) d\boldsymbol{\theta}$ is the time-independent probability density function of A . Therefore, we will use the dynamics of $G(A, t)$ as a proxy to justify the QSS hypothesis.

We used the ResNet-18 architecture as our NN model for the classification task of the CIFAR-10 dataset. We trained 1000 models using random initialization and plotted the test accuracy as a function of the number of epochs, which we will refer to as trajectories. We used standard SGD training, without perturbations. See the Computational Details section for the full training setup. To obtain the propagator $G(A, t)$ from the trajectory data for a specific target test accuracy, we treat it as an absorbing boundary. In other words, trajectories that reached the target accuracy are stopped and excluded from $G(A, t)$ at later times. The survival $\Psi_T(t)$ is estimated by the fraction of models that did not reach the target at epoch t of the training, i.e.,

$$\Psi_T(t) = \Pr(T > t) \approx \frac{1}{N} \sum_{i=1}^N \mathcal{I}_i(t), \quad (12)$$

where N is the total number of sampled trajectories and $\mathcal{I}_i(t)$ is an indicator function which gives 1 if the i -th trajectory did not reach the target before time t . In Fig. 3A, we start by analyzing the specific case of a target test accuracy of 75% (dashed blue line). For this accuracy, no model reaches the target up to 100 epochs, i.e., $\Psi_T(t) = 1 \forall t$ (blue line Fig. 3C). The violins of Fig. 3A represent the density distribution of A as a function of time. It narrows down with time, until epoch ~ 20 , and then remains with a fixed shape and height, which suggests that $G(A, t) = \phi(A)$ from that epoch onwards. Besides this qualitative shape comparison, we also quantitatively compare the cumulative distribution functions (CDFs) of A to the average CDF of A over epochs 20 to 100 with the Kolmogorov–Smirnov (KS) test [59–61], shown in Fig. 3D (blue line). We define the relaxation time as having a p-value larger than 0.05 in the KS test, which gives a relaxation time of $t_r = 17$ epochs. Alternative statistical tests result in similar relaxation times (see the supporting information).

In Fig. 3B we set the target test accuracy to 72% which leads to a decay of $\Psi_T(t)$ with the number of epochs, i.e., some trajectories reach the target during the training (orange line in Fig. 3C). Although there is a decline in the number of models that did not reach the target, after ~ 30 epochs the shape of the density distribution again remains approximately fixed while the height decreases, as expected from a QSS (Eq. (11)). We compare the CDFs of A to the average CDF of A over epochs 20 to 100 with the KS test [59–61], conditioned on model survival. Similarly to the previous case, we plot the p-value of the KS-test in Fig. 3D (orange line) and obtain

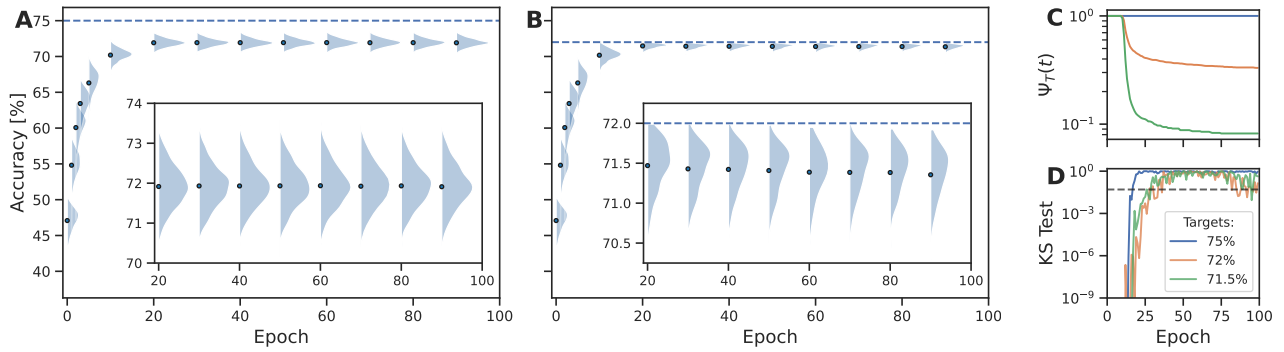


Figure 3. Experimental evidence for a quasi-steady-state. Panels A and B are violin plots of the density distributions of the test accuracy as a function of the number of epochs, for models that did not reach the target. Blue dots represent the mean accuracy and the blue areas are the distributions rotated by 90° . The dashed blue lines are the target accuracies, set to 75% and 72% in panels A and B, respectively. In both cases, after ~ 20 -30 epochs, the system reaches a QSS, i.e., $G(A, t) \simeq \phi(A)\Psi_T(t)$. Panel A is a special case in which $\Psi_T(t) = 1$, while in panel B, $\Psi_T(t)$ decays slowly. Panel C shows the survivals $\Psi_T(t)$ for the 75% (blue), 72% (orange), and 71.5% (green) target test accuracies. Panel D is the Kolmogorov–Smirnov (KS) test between the CDFs of the accuracy A at different epochs to the average CDF of A over epochs 20 to 100.

$t_r = 28$ epochs. We also checked the QSS hypothesis for a lower target accuracy of 71.5% and plot the survival function and KS-test p-value in Fig. 3C,D (green lines), respectively. Again, we obtain a similar relaxation time of $t_r = 26$ epochs.

All these examples are consistent with our hypothesis that the training of a CIFAR-10 classifier using a ResNet-18 model reaches a QSS for various target accuracies. Moreover, we find that the QSS is not a unique feature of the CIFAR-10 dataset and ResNet-18 architecture. We tested a different dataset, network architecture, and optimizer and found a QSS in all cases (See section E in the SI). We even demonstrate a QSS for a regression task similar to that of Dekel et al. [62].

C. Experimental test that the residual time is P -independent

We now show that if P is large enough, introducing a perturbation would result in P -independent residual times, according to Eq. (8). Here, we show it experimentally by focusing on the 72% target test accuracy case (Fig. 3B) where the system reaches a QSS after $t_r = 28$ epochs. We analyze the dependence of the residual time to reach the target on the perturbation time P . To do so, we take only the models that did not reach the target after $P = 100, 50, 20$, and 10 epochs, introduce the perturbation, and continue the training until reaching the target. We consider two perturbations, S&P and partial SR.

The S&P perturbation takes the weights and biases of the NN at the moment it is applied, shrinks them by a factor λ and adds an independent and identically distributed copy sampled from the initial conditions distribution, multiplied by a factor γ . We used the same values as in ref. [25], $\lambda = 0.4$ and $\gamma = 0.1$. The partial SR perturbation takes only a fraction of the parameters of the NN and re-initializes them to an independent and identically distributed copy sampled from the initial conditions distribution. Since small weights may contribute less to the performance of the model, their re-initialization holds the potential of escaping local minima while not throwing away most of the learned weights. We chose to initialize 30% of the weights, those with the smallest absolute value at the moment the perturbation is applied.

In Fig. 4, we first plot the mean test accuracy of the models as a function of the epoch. The top and bottom rows correspond to the S&P and the partial resetting perturbations, respectively. In all cases, we find that the residual time of the mean trajectory to reach the target is smaller than P and that the perturbation is only applied once before reaching the target. As a result, when $P > t_r$, we expect that the mean residual time will be P -independent, as explained in Section III A. In panels E and J we center all the mean trajectories with respect to their perturbation time P . We find that all curves approximately collapse on top of each other regardless of P , reaching the target accuracy after the same number of epochs since the perturbation has been applied (gray

area). We emphasize that the residual time is different for the two perturbations, as shown in panels E and J, but is P -independent in both cases.

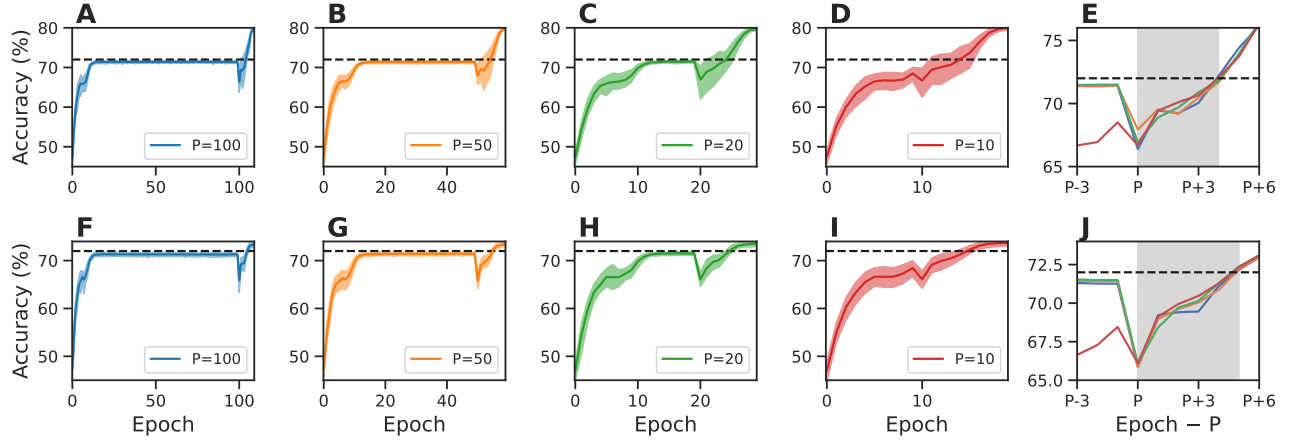


Figure 4. The mean trajectory of the test accuracy and its top and bottom deciles (shaded areas), for models that did not reach the target after P epochs. From left to right $P = 100, 50, 20, 10$ (see legend). The dashed black lines represent 72% test accuracy (the target). At epoch number P we apply the S&P protocol (upper row, panels A-E) or the partial SR protocol (bottom row, panels F-J). Panels E and J center the mean trajectories with respect to their P . The gray areas are from the moment of perturbation until the first time that the average trajectory reaches the target accuracy.

Next, instead of plotting the average training curve, we plot the value of the mean residual time $\bar{\tau}_P$ as a function of P in Fig. 5 for a larger range of $P = 1-100$. We observe that $\bar{\tau}_P$ is roughly constant over nearly two orders of magnitude in P for both perturbations. Surprisingly, $\bar{\tau}_P \approx \bar{\tau}$ even for values of P that are smaller than the relaxation time, beyond the expected range according to Eq. (8). However, when P becomes smaller than the residual time (~ 3 and ~ 5 for S&P and partial SR, respectively), denoted by the shaded area in Fig. 5, the process is perturbed more than once on average before reaching the target and the residual time is no longer P -independent. We observed the same behavior for different datasets and tasks presented in Section E of the supporting information.

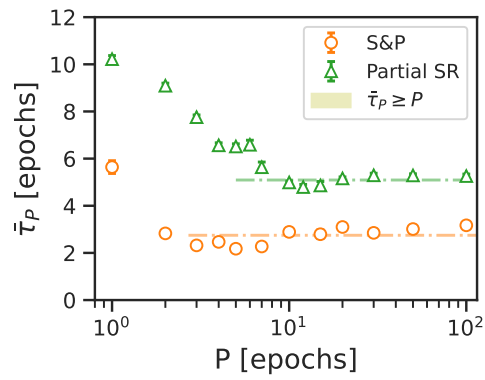


Figure 5. The mean residual time $\bar{\tau}_P$ versus the perturbation time. The values of $\bar{\tau}_P$ for S&P (orange circles) and partial SR (green triangles) are approximately constant when $P > \bar{\tau}_P$ (outside the yellow area). Dashed dotted lines are averages of all $\bar{\tau}_P < P$.

D. Prediction of the mean FPT

In this section, we show how to predict the mean FPT with a perturbation for a wide range of P from as few experiments as possible. We begin by assuming that several training trajectories are already available, and we wish to assess whether applying a perturbation is worthwhile, and select at what time interval to apply it. The simplest perturbation to analyze is SR. It comes at no additional cost, through Eq. (5), since we already sampled the survival function. To quantify the acceleration in reaching a target accuracy by applying a perturbation, we define the speedup as the ratio between the mean FPT without and with the perturbation, respectively. We plot the predicted speedup for SR in Fig. 6 (blue line) and compare it with numerical experiments (blue squares). We find that SR leads to a maximal speedup of ~ 3 using a perturbation time interval of ~ 20 .

To go beyond SR to other perturbations that could potentially lead to higher speedups, we must measure their residual time. A naive approach of simply evaluating $\bar{\tau}_P$ for every P and using Eq. (3) would mean running the training for all perturbations at all P values, which is costly. Instead, we would like to use the fact that the residual time is P -independent. To that end, we sample the training with the perturbation applied once at some P^* that is large enough. We then use Eq. (9) to predict the mean FPT for a wide range of $P < P^*$. We plot the predicted speedup in Fig. 6 for the S&P (orange line) and partial SR (green line) perturbations, using their value of $\bar{\tau}_{P^*}$ at $P^* = 100$. Going from right to left on the P axis, the predictions fit the experimental values of the S&P (orange circles) and partial SR (green triangles) protocols for $P \geq \bar{\tau}_{P^*}$, as expected.

Using these predictions, we identify that S&P leads to a speedup of ~ 16 at a perturbation time interval of 3, while partial SR leads to a speedup of ~ 8 at $P = 7$. These predictions correctly identify S&P as the preferred strategy that leads to the highest speedup. Although the experimental maximal speedup is slightly larger (~ 21), our predictions are a computationally efficient way of determining useful perturbations and time intervals that lead to high speedups.

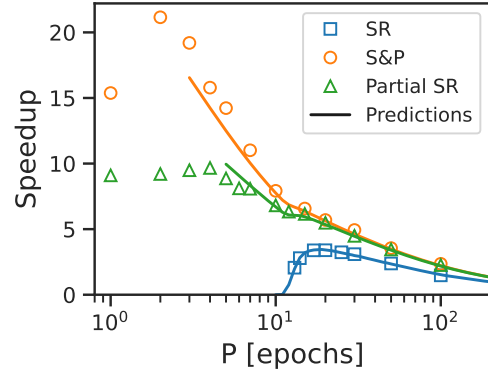


Figure 6. The speedup gained by using different perturbation protocols versus the perturbation time. Orange and green solid lines are the theoretical predictions of Eq. (9) for S&P and partial SR, respectively. For the predictions, we used the value of $\bar{\tau}_{P^*}$ for $P^* = 100$. We plot the predictions only down to $P = \bar{\tau}_{P^*}$. The blue solid line is the theoretical prediction for the SR case (Eq. (5)). Symbols represent averages over brute force training at every value of P .

We suggest a general methodology that can examine different kinds of perturbations and pick the optimal one and an efficient P . Consider for example a classification task for which the architecture of the NN and the hyperparameters of the SGD-based optimization are given. Then, it is common practice to train in parallel an ensemble of models and terminate any training process that did not reach a minimal desired test accuracy after a tolerance time of P^* epochs. After this process is completed, we propose to estimate the survival function, $\Psi_T(t)$ for $t \leq P^*$ obtained by Eq. (12). This is already enough information to evaluate whether SR leads to any acceleration. For other perturbations, evaluate first if the training accuracy of the unperturbed process reaches a QSS and determine $t_r < P^*$ using the KS test. If that is the case, introduce several candidate perturbations to the models that did not reach the target accuracy and measure $\bar{\tau}_{P^*}$ for each one. This way, $\Psi_T(t \leq P^*)$ and $\bar{\tau}_{P^*}$ are obtained simultaneously for several perturbation protocols. According to Eq. (9), the perturbation with the

minimal $\bar{\tau}_{P^*}$ is the preferred one. Finally, to obtain an efficient perturbation time interval, plug $\Psi_T(t \leq P^*)$ and $\bar{\tau}_{P^*}$ into Eq. (9), and evaluate the speedup for $\max(t_r, \bar{\tau}_{P^*}) \leq P \leq P^*$. Choose the time interval that leads to the highest speedup. In conclusion, if one plans to estimate the MFPT for a perturbation at a single rate, they might as well use our approach to predict whether lower rates would lead to higher accelerations at almost no added computational cost.

IV. SUMMARY AND CONCLUSION

We developed an approach based on a recent response theory by Keidar et al. [38] to design useful perturbations for accelerating the training of NNs. To that end, we treated the training as a first-passage process to a target test accuracy. For the case of a CIFAR-10 classifier using the ResNet-18 architecture, we demonstrated that the unperturbed training test accuracy reached a QSS after a relaxation time of 20-30 epochs. We showed that, as a result, we can predict the mean FPT for a wide range of perturbation times from measurements at a single perturbation time. We focused on three perturbations: S&P, SR and partial SR, but our method is general and can be used for other perturbations. Lastly, we proposed a strategy to examine different kinds of perturbations and pick the optimal one and an efficient P . We showed that this strategy correctly selects S&P as a better perturbation than partial SR or SR for a CIFAR-10 classifier and identified a useful perturbation time. We demonstrated the transferability of the methodology to other datasets, architectures, optimizers and even tasks (regression instead of classification). Our work provides a first-passage framework capable of identifying perturbations that result in a speedup when training an NN model up to a target accuracy. It allows for a more rational design of perturbation protocols, based on physical insights.

V. COMPUTATIONAL DETAILS

The CIFAR-10 dataset contains 50,000 training and 10,000 test RGB images each belonging to one of 10 different classes. The number of images per class across the train and test sets is equal, and each image is 32×32 pixels in size. For classification, we used a common modified version of the ResNet-18 architecture, because the original architecture was designed for much larger images. The modification includes reducing the kernel size of the first convolution layer from 7 to 3, the stride from 2 to 1, and the padding from 3 to 1. We also removed the subsequent max pooling layer to maintain everything else similar to the original architecture (as was done in the work of Zaidi et al. [25]).

We did not use any data augmentation techniques except for standard data normalization (by the channel-wise mean and variance of the train images) for both train and test datasets. We initialized the weights and biases with the default initialization of Pytorch, i.e., uniform distribution, and used the FFCV library for faster training [63]. We trained each model with an SGD optimizer with a learning rate of 0.02 and batch size of 125. Implementation of the perturbations was straightforward according to their definitions above. The test accuracy curves for each perturbative protocol with $P = 20$ are presented in supporting information.

Raw data and example code to train the models and make the predictions are given in the associated repository: <https://github.com/Hirshberg-Lab/0ptPerturbationsNN>

ACKNOWLEDGEMENTS

B.H. acknowledges support from the Israel Science Foundation (grants No. 1037/22 and 1312/22), the Pazy Foundation of the IAEC-UPBC (grant No. 415-2023), and Tel Aviv University Center for Artificial Intelligence and Data Science (TAD). This project has received funding from the European Research Council (ERC) under the European Union’s Horizon 2020 research and innovation program (grant agreement No. 947731 to S.R.). S.M. acknowledges support from the Quantum Science and Technology Center of Tel Aviv University. B.H. and S.M. thank Sheheryar Zaidi for sharing his code. The authors thank Yohai Bar Sinai, Tomer Koren, and Rotem Widman

for fruitful discussions.

- [1] J. Jumper, R. Evans, A. Pritzel, T. Green, M. Figurnov, O. Ronneberger, K. Tunyasuvunakool, R. Bates, A. Žídek, A. Potapenko, *et al.*, Highly accurate protein structure prediction with alphafold, *Nature* **596**, 583 (2021).
- [2] A. Nir, E. Sela, R. Beck, and Y. Bar-Sinai, Machine-learning iterative calculation of entropy for physical systems, *Proceedings of the National Academy of Sciences* **117**, 30234 (2020).
- [3] J. Behler and M. Parrinello, Generalized neural-network representation of high-dimensional potential-energy surfaces, *Physical review letters* **98**, 146401 (2007).
- [4] G. Carleo and M. Troyer, Solving the quantum many-body problem with artificial neural networks, *Science* **355**, 602 (2017).
- [5] F. Noé, S. Olsson, J. Köhler, and H. Wu, Boltzmann generators: Sampling equilibrium states of many-body systems with deep learning, *Science* **365**, eaaw1147 (2019).
- [6] B. Máté, F. Fleuret, and T. Bereau, Neural thermodynamic integration: Free energies from energy-based diffusion models, *The Journal of Physical Chemistry Letters* **15**, 11395 (2024).
- [7] A. Anelli, H. Dietrich, P. Ectors, F. Stowasser, T. Bereau, M. Neumann, and J. van den Ende, Robust and efficient reranking in crystal structure prediction: a data driven method for real-life molecules, *CrystEngComm* **26**, 5845 (2024).
- [8] C. Lagemann, K. Lagemann, S. Mukherjee, and W. Schröder, Deep recurrent optical flow learning for particle image velocimetry data, *Nature Machine Intelligence* **3**, 641 (2021).
- [9] S. Ravuri, K. Lenc, M. Willson, D. Kangin, R. Lam, P. Mirowski, M. Fitzsimons, M. Athanassiadou, S. Kashem, S. Madge, *et al.*, Skilful precipitation nowcasting using deep generative models of radar, *Nature* **597**, 672 (2021).
- [10] Y. Wang, J. M. L. Ribeiro, and P. Tiwary, Machine learning approaches for analyzing and enhancing molecular dynamics simulations, *Current opinion in structural biology* **61**, 139 (2020).
- [11] M. Rupp, A. Tkatchenko, K.-R. Müller, and O. A. Von Lilienfeld, Fast and accurate modeling of molecular atomization energies with machine learning, *Physical review letters* **108**, 058301 (2012).
- [12] S.-T. Tsai, E.-J. Kuo, and P. Tiwary, Learning molecular dynamics with simple language model built upon long short-term memory neural network, *Nature communications* **11**, 5115 (2020).
- [13] P. Geiger and C. Dellago, Neural networks for local structure detection in polymorphic systems, *The Journal of chemical physics* **139** (2013).
- [14] K. Fukumizu and S.-i. Amari, Local minima and plateaus in hierarchical structures of multilayer perceptrons, *Neural networks* **13**, 317 (2000).
- [15] I. Loshchilov and F. Hutter, Sgdr: Stochastic gradient descent with warm restarts, *arXiv preprint arXiv:1608.03983* (2016).
- [16] D. E. Rumelhart, G. E. Hinton, and R. J. Williams, Learning representations by back-propagating errors, *nature* **323**, 533 (1986).
- [17] X. Peng, L. Li, and F.-Y. Wang, Accelerating minibatch stochastic gradient descent using typicality sampling, *IEEE transactions on neural networks and learning systems* **31**, 4649 (2019).
- [18] J. Duchi, E. Hazan, and Y. Singer, Adaptive subgradient methods for online learning and stochastic optimization., *Journal of machine learning research* **12** (2011).
- [19] M. D. Zeiler, Adadelta: an adaptive learning rate method, *arXiv preprint arXiv:1212.5701* (2012).
- [20] D. P. Kingma, Adam: A method for stochastic optimization, *arXiv preprint arXiv:1412.6980* (2014).
- [21] G. Nguyen, S. Dlugolinsky, M. Bobák, V. Tran, Á. López García, I. Heredia, P. Malík, and L. Hluchý, Machine learning and deep learning frameworks and libraries for large-scale data mining: a survey, *Artificial Intelligence Review* **52**, 77 (2019).
- [22] I. Sutskever, J. Martens, G. Dahl, and G. Hinton, On the importance of initialization and momentum in deep learning, in *International conference on machine learning* (PMLR, 2013) pp. 1139–1147.
- [23] B. Leimkuhler, C. Matthews, and T. Vlaar, Partitioned integrators for thermodynamic parameterization of neural networks, *Foundations of Data Science* **1**, 457 (2019).
- [24] J. Ash and R. P. Adams, On warm-starting neural network training, *Advances in neural information processing systems* **33**, 3884 (2020).
- [25] S. Zaidi, T. Berariu, H. Kim, J. Bornschein, C. Clopath, Y. W. Teh, and R. Pascanu, When does re-initialization work?, in *Proceedings on* (PMLR, 2023) pp. 12–26.
- [26] Y. Bae, Y. Song, and H. Jeong, Stochastic resetting mitigates latent gradient bias of sgd from label noise, *Machine Learning: Science and Technology* **6**, 015062 (2025).
- [27] S. Dohare, J. F. Hernandez-Garcia, Q. Lan, P. Rahman, A. R. Mahmood, and R. S. Sutton, Loss of plasticity in deep continual learning, *Nature* **632**, 768 (2024).
- [28] Y. Feng and Y. Tu, The inverse variance–flatness relation in stochastic gradient descent is critical for finding flat minima, *Proceedings of the National Academy of Sciences* **118**, e2015617118 (2021).

[29] X. Cheng, D. Yin, P. Bartlett, and M. Jordan, Stochastic gradient and langevin processes, in *International Conference on Machine Learning* (PMLR, 2020) pp. 1810–1819.

[30] T. Jules, G. Brener, T. Kachman, N. Levi, and Y. Bar-Sinai, Charting the topography of the neural network landscape with thermal-like noise, arXiv preprint arXiv:2304.01335 (2023).

[31] A. A. Alemi and I. Fischer, Therml: Thermodynamics of machine learning, arXiv preprint arXiv:1807.04162 (2018).

[32] H. S. Seung, H. Sompolinsky, and N. Tishby, Statistical mechanics of learning from examples, *Physical review A* **45**, 6056 (1992).

[33] A. Choromanska, M. Henaff, M. Mathieu, G. B. Arous, and Y. LeCun, The loss surfaces of multilayer networks, in *Artificial intelligence and statistics* (PMLR, 2015) pp. 192–204.

[34] L. Zdeborová, Understanding deep learning is also a job for physicists, *Nature Physics* **16**, 602 (2020).

[35] G. E. Karniadakis, I. G. Kevrekidis, L. Lu, P. Perdikaris, S. Wang, and L. Yang, Physics-informed machine learning, *Nature Reviews Physics* **3**, 422 (2021).

[36] G. Carleo, I. Cirac, K. Cranmer, L. Daudet, M. Schuld, N. Tishby, L. Vogt-Maranto, and L. Zdeborová, Machine learning and the physical sciences, *Reviews of Modern Physics* **91**, 045002 (2019).

[37] M. Stephan, M. D. Hoffman, and D. M. Blei, Stochastic gradient descent as approximate bayesian inference, *Journal of Machine Learning Research* **18**, 1 (2017).

[38] T. D. Keidar and S. Reuveni, Universal linear response of the mean first-passage time, arXiv preprint arXiv:2410.16129 (2024).

[39] S. Redner, *A Guide to First-Passage Processes* (Cambridge University Press, 2001).

[40] R. Metzler, S. Redner, and G. Oshanin, *First-passage phenomena and their applications*, Vol. 35 (World Scientific, 2014).

[41] A. J. Bray, Satya N. Majumdar, and G. Schehr, Persistence and first-passage properties in nonequilibrium systems, *Advances in Physics* **62**, 225 (2013).

[42] A. Krizhevsky, G. Hinton, et al., *Learning multiple layers of features from tiny images*, Master's thesis, Toronto, ON, Canada (2009).

[43] L. Deng, The mnist database of handwritten digit images for machine learning research, *IEEE Signal Processing Magazine* **29**, 141 (2012).

[44] K. He, X. Zhang, S. Ren, and J. Sun, Deep residual learning for image recognition, in *Proceedings of the IEEE conference on computer vision and pattern recognition* (2016) pp. 770–778.

[45] S. Reuveni, Optimal stochastic restart renders fluctuations in first passage times universal, *Physical review letters* **116**, 170601 (2016).

[46] A. Pal and S. Reuveni, First passage under restart, *Physical review letters* **118**, 030603 (2017).

[47] M. R. Evans, S. N. Majumdar, and G. Schehr, Stochastic resetting and applications, *Journal of Physics A: Mathematical and Theoretical* **53**, 193001 (2020).

[48] O. Blumer, S. Reuveni, and B. Hirshberg, Stochastic resetting for enhanced sampling, *The journal of physical chemistry letters* **13**, 11230 (2022).

[49] O. Blumer, S. Reuveni, and B. Hirshberg, Combining stochastic resetting with metadynamics to speed-up molecular dynamics simulations, *Nature Communications* **15**, 240 (2024).

[50] I. Eliazar and S. Reuveni, Mean-performance of sharp restart i: statistical roadmap, *Journal of Physics A: Mathematical and Theoretical* **53**, 405004 (2020).

[51] A. Nitzan, *Chemical dynamics in condensed phases: relaxation, transfer, and reactions in condensed molecular systems* (Oxford university press, 2024).

[52] W. Ji, W. Qiu, Z. Shi, S. Pan, and S. Deng, Stiff-pinn: Physics-informed neural network for stiff chemical kinetics, *The Journal of Physical Chemistry A* **125**, 8098 (2021).

[53] H. A. Kramers, Brownian motion in a field of force and the diffusion model of chemical reactions, *physica* **7**, 284 (1940).

[54] P. Hanggi, Escape from a metastable state, *Journal of Statistical Physics* **42**, 105 (1986).

[55] P. Hänggi, P. Talkner, and M. Borkovec, Reaction-rate theory: fifty years after kramers, *Reviews of modern physics* **62**, 251 (1990).

[56] A. Barducci, M. Bonomi, and M. Parrinello, Metadynamics, *Wiley Interdisciplinary Reviews: Computational Molecular Science* **1**, 826 (2011).

[57] O. Valsson and M. Parrinello, Variational approach to enhanced sampling and free energy calculations, *Physical review letters* **113**, 090601 (2014).

[58] G. Bussi and A. Laio, Using metadynamics to explore complex free-energy landscapes, *Nature Reviews Physics* **2**, 200 (2020).

[59] F. J. Massey Jr, The kolmogorov-smirnov test for goodness of fit, *Journal of the American statistical Association* **46**, 68 (1951).

[60] P. Tiwary, J. Mondal, J. A. Morrone, and B. Berne, Role of water and steric constraints in the kinetics of cavity–ligand unbinding, *Proceedings of the National Academy of Sciences* **112**, 12015 (2015).

[61] O. Blumer, S. Reuveni, and B. Hirshberg, Short-time infrequent metadynamics for improved kinetics inference, *Journal of Chemical Theory and Computation* **20**, 3484 (2024).

- [62] S. Dekel and L. Gugel, Pr-dad: Phase retrieval using deep auto-decoders, in *2022 7th International Conference on Frontiers of Signal Processing (ICFSP)* (IEEE, 2022) pp. 165–172.
- [63] G. Leclerc, A. Ilyas, L. Engstrom, S. M. Park, H. Salman, and A. Mądry, Ffcv: Accelerating training by removing data bottlenecks, in *Proceedings of the IEEE/CVF Conference on Computer Vision and Pattern Recognition* (2023) pp. 12011–12020.

SUPPORTING INFORMATION: FIRST-PASSAGE APPROACH TO OPTIMIZING PERTURBATIONS FOR IMPROVED TRAINING OF MACHINE LEARNING MODELS

A. Derivation of Eq. 3 of the main text

This appendix shows the derivation of Eq. (3). Note that a similar derivation is presented in [38], but for exponentially distributed perturbation times instead of a constant P . Using the law of total expectation on Eq. (2), the mean FPT is,

$$\mathbb{E}[T_P] = \Pr(T \leq P)\mathbb{E}[T \mid T \leq P] + \Pr(T > P)(\mathbb{E}[P \mid T > P] + \mathbb{E}[\mathbb{E}[\tau_P(\boldsymbol{\theta})] \mid T > P]). \quad (\text{S1})$$

We define

$$\bar{\tau}_P \equiv \mathbb{E}[\mathbb{E}[\tau_P(\boldsymbol{\theta})] \mid T > P] = \int_{\Theta} \mathbb{E}[\tau_P(\boldsymbol{\theta})] \frac{G(\boldsymbol{\theta}, P)}{\Pr(T > P)} d\boldsymbol{\theta} = \int_{\Theta} \mathbb{E}[\tau_P(\boldsymbol{\theta})] \frac{G(\boldsymbol{\theta}, P)}{\Psi_T(P)} d\boldsymbol{\theta}, \quad (\text{S2})$$

as taking the expectation value of $\tau_P(\boldsymbol{\theta})$ first over all possible noise realizations of the stochastic training process after the perturbation was applied to a given state $\boldsymbol{\theta}$ at time P , and then over all possible $\boldsymbol{\theta}$ generated by the unperturbed process at time P right before the perturbation has been applied. The mean FPT with the perturbation is then given by

$$\mathbb{E}[T_P] = \Pr(T \leq P)\mathbb{E}[T \mid T \leq P] + \Pr(T > P)(\mathbb{E}[P \mid T > P] + \bar{\tau}_P). \quad (\text{S3})$$

Next, we write the survival function $\Psi_T(t)$ in terms of the probability mass function of T , $\mathcal{P}_T(t)$,

$$\Psi_T(t) = \Pr(T > t) = 1 - \sum_{n=0}^t \mathcal{P}_T(n), \quad (\text{S4})$$

such that $\mathcal{P}_T(t) = \Psi_T(t-1) - \Psi_T(t)$. With this definition, we can compute each conditional expectation in Eq. (S3). The first term is,

$$\mathbb{E}[T \mid T \leq P] = \frac{1}{\Pr(T \leq P)} \sum_{t=0}^P t \mathcal{P}_T(t), \quad (\text{S5})$$

where the normalization factor is $\Pr(T \leq P)$ due to the conditional average. Since the first term in the sum is zero, we get

$$\mathbb{E}[T \mid T \leq P] = \frac{1}{\Pr(T \leq P)} \sum_{t=1}^P t \mathcal{P}_T(t) = \frac{1}{\Pr(T \leq P)} \sum_{t=1}^P t(\Psi_T(t-1) - \Psi_T(t)). \quad (\text{S6})$$

By changing the summation index of the first sum, we can rewrite

$$\mathbb{E}[T \mid T \leq P] = \frac{1}{\Pr(T \leq P)} \left(\sum_{t=0}^{P-1} (t+1) \Psi_T(t) - \sum_{t=1}^P t \Psi_T(t) \right) = \frac{1}{\Pr(T \leq P)} \left(\sum_{t=0}^{P-1} \Psi_T(t) - P \Psi_T(P) \right), \quad (\text{S7})$$

which is the final expression for the first expectation value. The second term is,

$$\mathbb{E}[P \mid T > P] = P = \frac{P \Psi_T(P)}{\Pr(T > P)}. \quad (\text{S8})$$

Plugging these two terms back into Eq. (S3),

$$\mathbb{E}[T_P] = \sum_{t=0}^{P-1} \Psi_T(t) - \cancel{P \Psi_T(P)} + \cancel{P \Psi_T(P)} + \Psi_T(P) \bar{\tau}_P, \quad (\text{S9})$$

results in Eq. (3).

B. Computational details of testing the QSS hypothesis

This appendix includes computational details and provides additional support for the QSS of the test accuracy during SGD training without perturbations. The CDF $F_t(A)$ of the accuracy A at epoch t was calculated according to,

$$F_t(A) = \frac{1}{N(t)} \sum_{i=1}^{N(t)} I\{A_i(t) \leq A\}. \quad (\text{S10})$$

Here, $N(t)$ is the number of models that did not reach the target accuracy at time t , $I\{E\}$ is the indicator function of the event E , and $A_i(t)$ is the accuracy of the i -th model at time t . The average CDF $\bar{F}(A)$ of A over epochs 20 to 100 was taken as an arithmetic average of the accuracy CDFs, i.e.,

$$\bar{F}(A) = \frac{1}{t_2 - t_1 + 1} \sum_{t=t_1}^{t_2} F_t(A). \quad (\text{S11})$$

C. Other statistical tests

In Fig. S1 we plot the CDFs of the test accuracy versus the values of the mean CDF of A over epochs 20 to 100. The mean CDF is plotted in black for qualitative comparison between other CDFs (see legend).

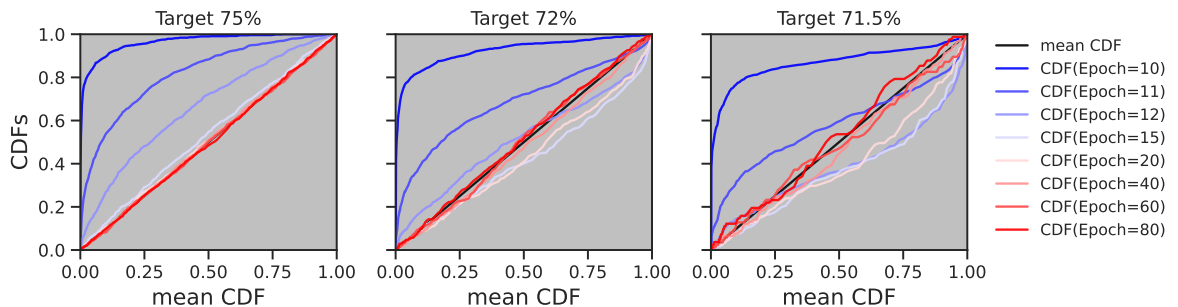


Figure S1. CDFs versus the mean CDF. Blue and red colors indicate CDFs before and after reaching a QSS respectively.

In Fig. S2 we compare the CDFs of the test accuracy A to the average CDF of A over epochs 20 to 100 with another measure, the Cramér–von Mises (CM) criterion. The CM criterion at epoch t is calculated as follows,

$$CM(t) = \int_0^1 (F_t(A) - \bar{F}(A))^2 d\bar{F}(A). \quad (\text{S12})$$

Here, $\bar{F}(A)$ is the average CDF of A over epochs 20 to 100. In practice, we take the square of the difference between each curve of Fig. S1 and the mean CDF, and integrate along the x-axis.

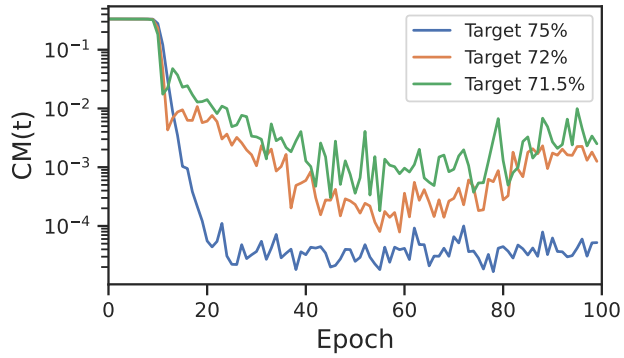


Figure S2. Cramér–von Mises criterion

D. Training with and without perturbations

This appendix shows in Fig. S3 the mean test accuracy curves of standard SGD training (black), and training with SR (blue), S&P (orange), and partial SR (green).

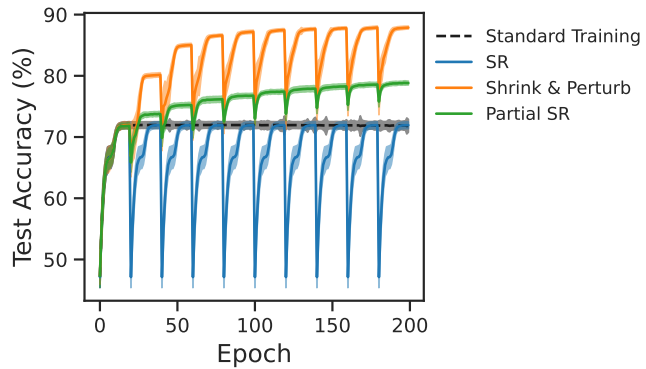


Figure S3. Test accuracy of different training protocols with perturbation time $P = 20$ epochs. Standard training in black, SR in blue, S&P in orange, and partial SR in green.

E. Transferability across datasets, optimizers, architectures and tasks

In this section, we demonstrate that the QSS is not a unique feature of the CIFAR-10 and ResNet-18 dataset and architecture. We test additional datasets, architecture, optimizer, and even task (classification versus regression). The following subsections show three experimental tests: 1) CIFAR-100 classification with all other hyperparameters and setting as in the main text, 2) CIFAR-100 classification, but using SGD with momentum, and 3) a regression phase retrieval task on the MNIST dataset [43] using a fully connected architecture and the Adam optimizer [20].

1. CIFAR-100 Classification

In Fig. S4, we show that the training process on the CIFAR-100 dataset also reaches a QSS. We used the same optimizer, architecture, and learning rate as was used for the CIFAR-10 dataset.

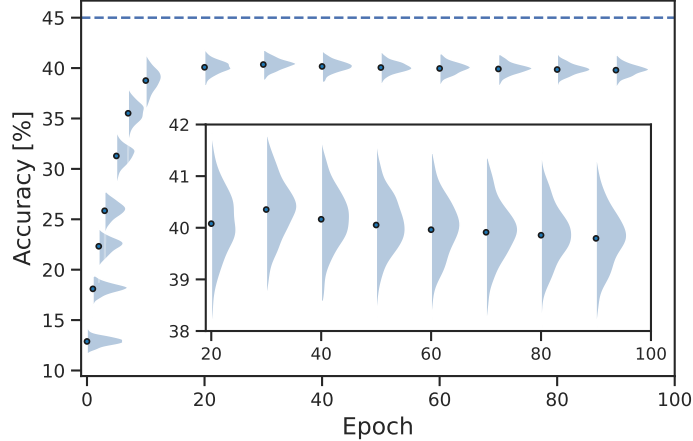


Figure S4. Experimental evidence for a quasi-steady-state on the CIFAR-100 dataset. In blue are violin plots of the density distributions of the test accuracy as a function of the number of epochs, for models that did not reach the target. Dots represent the mean accuracy and the areas are the distributions rotated by 90° . The dashed blue line is the target accuracy set to 45%.

Since the training process reaches a QSS we predict that $\bar{\tau}_P$ is independent of P for a wide range according to Eq. (9). To verify it, we applied the S&P perturbation to the training trajectories that did not reach the target prior to time P (see Fig. S5).

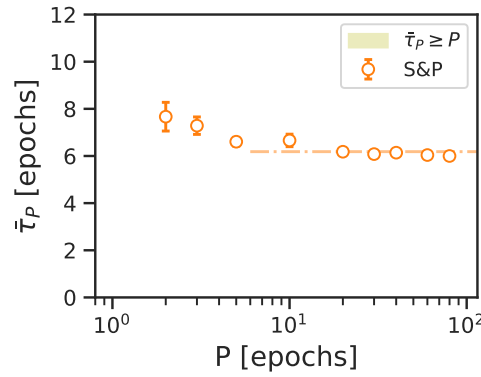


Figure S5. The mean residual time $\bar{\tau}_P$ to reach 45% test accuracy versus the perturbation time, for CIFAR-100 classification task. The values of $\bar{\tau}_P$ for S&P (orange circles) are approximately constant when $P > \bar{\tau}_P$ (outside the yellow area). Dashed dotted line is the average over all $\bar{\tau}_P < P$.

Finally, we predict the mean perturbed FPT $\mathbb{E}[T_P]$ to reach a target test accuracy of 45%, shown in Fig. S6.

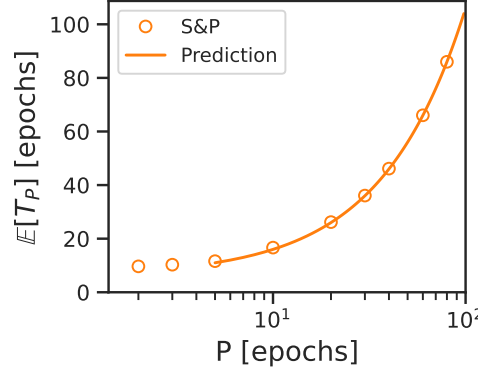


Figure S6. The perturbed mean FPT to reach 45% test accuracy on the CIFAR-100 classification. The orange line is the theoretical predictions of Eq. (9) for S&P. For the predictions, we used the value of $\bar{\tau}_{P^*}$ for $P^* = 80$.

2. CIFAR-100 classification - training with momentum

In Fig. S7, we show that the training process with a momentum term, on the CIFAR-100 dataset reaches a QSS. We used the same architecture and learning rate as was used for the CIFAR-10 dataset. We used a momentum value of 0.9.

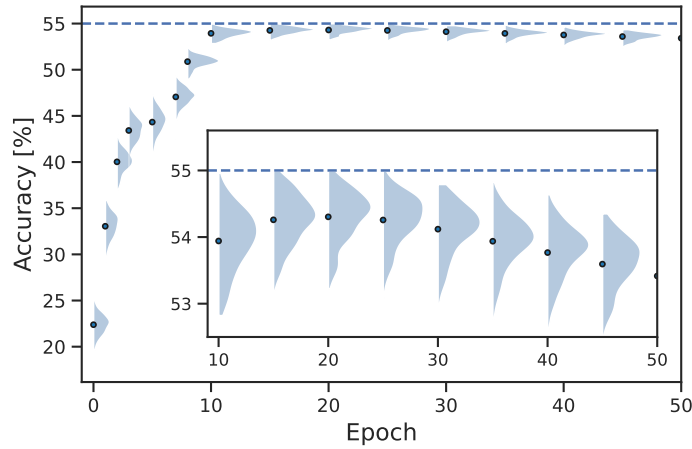


Figure S7. Experimental evidence for a quasi-steady-state on the CIFAR-100 dataset with momentum. In blue are violin plots of the density distributions of the test accuracy as a function of the number of epochs, for models that did not reach the target. Dots represent the mean accuracy and the areas are the distributions rotated by 90°. The dashed blue line is the target accuracy set to 55%.

Similarly to the case without momentum we show that $\bar{\tau}_P$ is independent of P for a wide range in Fig. S8.

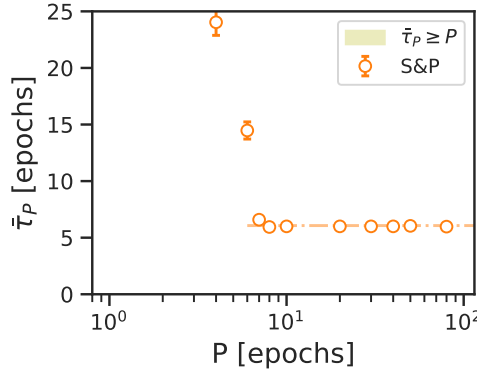


Figure S8. The mean residual time $\bar{\tau}_P$ to reach 55% test accuracy versus the perturbation time for the CIFAR-100 classification task when trained with momentum. The values of $\bar{\tau}_P$ for S&P (orange circles) are approximately constant when $P > \bar{\tau}_P$ (outside the yellow area). Dashed dotted line is the average over all $\bar{\tau}_P < P$.

Finally, we predict the mean perturbed FPT $\mathbb{E}[T_P]$ to reach a target test accuracy of 55%, shown in Fig. S9.

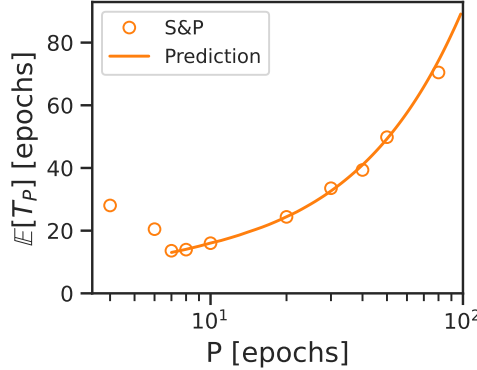


Figure S9. The perturbed mean FPT to reach 55% test accuracy on the CIFAR-100 classification with momentum. The orange line is the theoretical predictions of Eq. (9) for S&P. For the predictions, we used the value of $\bar{\tau}_{P^*}$ for $P^* = 50$.

3. Regression task - phase retrieval of images

To demonstrate a QSS for a regression task, we trained a fully-connected NN to reconstruct images from their Fourier-transformed magnitude, i.e., the absolute value of their Fourier transform. We used a similar problem setting as in Dekel et al. [62]. The input of the network is created by taking the absolute value over the Fourier transform of the MNIST images (see Fig. S10). The model learns to reconstruct the corresponding image by minimizing an L2 loss between its output and the ground truth image.

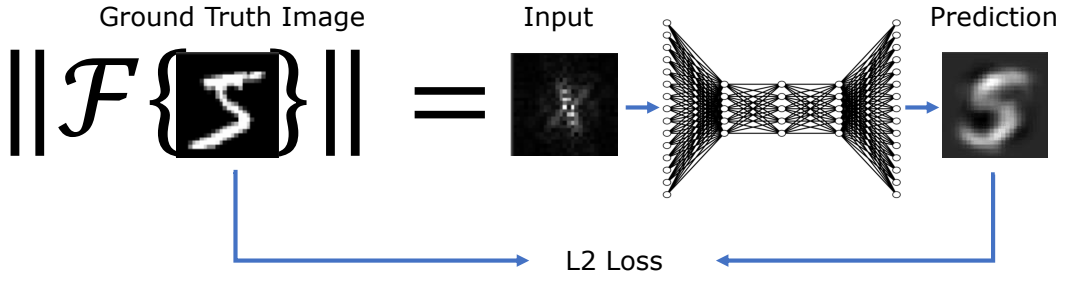


Figure S10. Example of the phase retrieval problem settings. We take the absolute value over the Fourier transform of the MNIST images, to create the inputs for the model. The model learns to reconstruct images from their magnitude by minimizing the L2 loss between the ground truth and the output images. We use an L2 loss that is invariant to 180° rotation.

To elevate the difficulty of this problem we swapped the roles between the test and train datasets of MNIST. We used the Adam optimizer with a learning rate of 0.1 and batch size of 1000. The architecture of our model contains four fully connected layers ($784 \times 256 \times 256 \times 784$). Between every two layers, there is a batch normalization layer followed by a parametric ReLU activation. Also, we used an L2 loss that is invariant to 180° rotation of the predicted image. This is because both images would have the same magnitude.

To demonstrate a QSS in the learning process of this regression task, we observe the distribution of the L2 test loss instead of “test accuracy” that was used for the classification tasks (see Fig. S11).

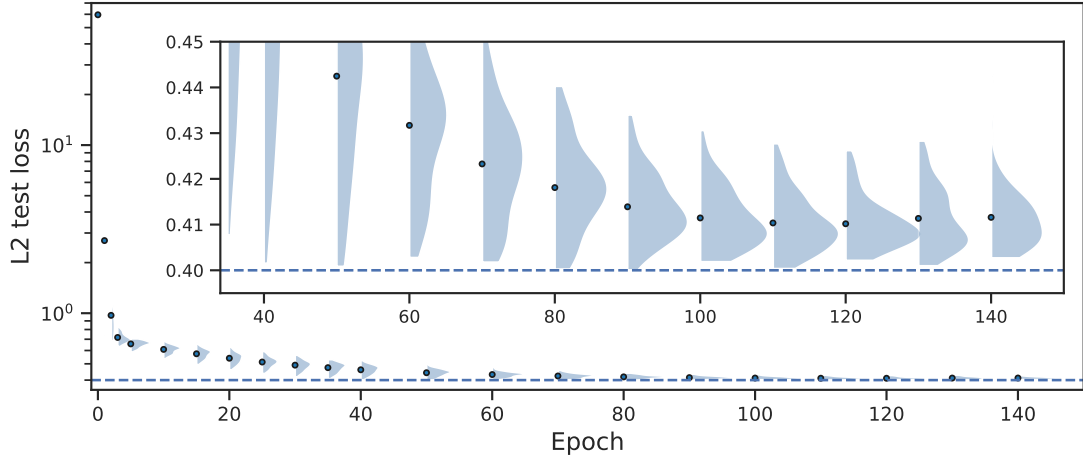


Figure S11. Experimental evidence for a quasi-steady-state for a regression task. The target was set on 0.4 L2 test loss.

As in the classification case, we demonstrate that $\bar{\tau}_P$ is independent of P for a wide range in Fig. S12. We used the S&P protocol but with different hyperparameters: $\lambda=0.8$ for shrinking and $\gamma=0.05$ for perturbing.

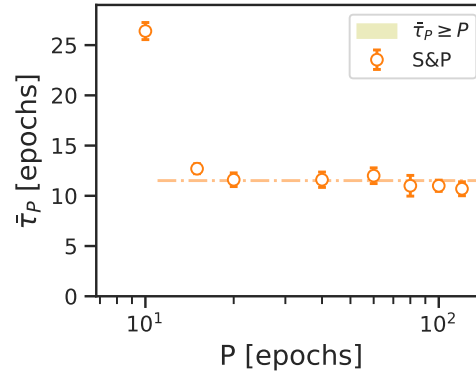


Figure S12. The mean residual time $\bar{\tau}_P$ versus the perturbation time for the regression task. The values of $\bar{\tau}_P$ for S&P (orange circles) are approximately constant when $P > \bar{\tau}_P$ (outside the yellow area). Dashed dotted line is the average over all $\bar{\tau}_P < P$.

Finally, we predict the mean perturbed FPT $\mathbb{E}[T_P]$ to reach a target loss value of 0.4, shown in Fig. S13.

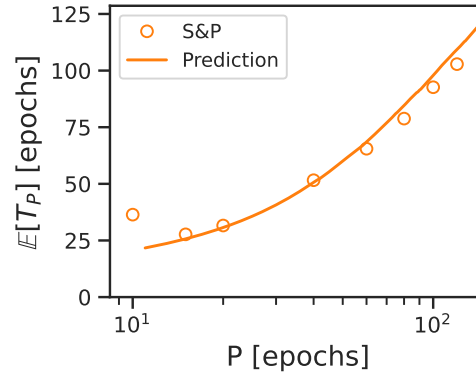


Figure S13. The perturbed mean FPT to reach 0.4 L2 test loss with the Adam optimizer for the regression task. The orange line is the theoretical prediction of Eq. (9) for S&P. For the predictions, we used the value of $\bar{\tau}_{P^*}$ for $P^* = 120$.